


# Effect of biomaterial stiffness on cardiac mechanics in a biventricular infarcted rat heart model with microstructural representation of in situ intramyocardial injectate

Y. D. Motchon<sup>1</sup> | Kevin L. Sack<sup>1,2</sup> | M. S. Sirry<sup>3</sup> | M. Kruger<sup>4</sup> |  
E. Pauwels<sup>5,6</sup> | D. Van Loo<sup>5,7</sup> | A. De Muynck<sup>5</sup> | L. Van Hoorebeke<sup>5</sup> |  
Neil H. Davies<sup>4</sup> | Thomas Franz<sup>1,8</sup> 

<sup>1</sup>Biomedical Engineering Research Centre, Division of Biomedical Engineering, Department of Human Biology, University of Cape Town, Cape Town, South Africa

<sup>2</sup>Department of Surgery, University of California at San Francisco, San Francisco, California, USA

<sup>3</sup>Department of Biomedical Engineering, School of Engineering and Computing, American International University, Al Jahra, Kuwait

<sup>4</sup>Cardiovascular Research Unit, MRC IUHRU, University of Cape Town, Cape Town, South Africa

<sup>5</sup>Centre for X-ray Tomography, Department of Physics and Astronomy, Ghent University, Ghent, Belgium

<sup>6</sup>Nuclear Medicine, University Hospitals Leuven, Leuven, Belgium

<sup>7</sup>XRE nv, Bollebergen 2B box 1, 9052, Ghent, Belgium

<sup>8</sup>Bioengineering Science Research Group, Faculty of Engineering and Physical Sciences, University of Southampton, Southampton, UK

## Correspondence

Y. D. Motchon and Thomas Franz, Division of Biomedical Engineering, Department of Human Biology, University of Cape Town, Observatory, Cape Town, South Africa.

## Abstract

Intramyocardial delivery of biomaterials is a promising concept for treating myocardial infarction. The delivered biomaterial provides mechanical support and attenuates wall thinning and elevated wall stress in the infarct region. This study aimed at developing a biventricular finite element model of an infarcted rat heart with a microstructural representation of an in situ biomaterial injectate, and a parametric investigation of the effect of the injectate stiffness on the cardiac mechanics. A three-dimensional subject-specific biventricular finite element model of a rat heart with left ventricular infarct and microstructurally dispersed biomaterial delivered 1 week after infarct induction was developed from ex vivo microcomputed tomography data. The volumetric mesh density varied between  $303 \text{ mm}^{-3}$  in the myocardium and  $3852 \text{ mm}^{-3}$  in the injectate region due to the microstructural intramyocardial dispersion. Parametric simulations were conducted with the injectate's elastic modulus varying from 4.1 to 405,900 kPa, and myocardial and injectate strains were recorded. With increasing injectate stiffness, the end-diastolic median myocardial fibre and cross-fibre strain decreased in magnitude from 3.6% to 1.1% and from  $-6.0\%$  to  $-2.9\%$ , respectively. At end-systole, the myocardial fibre and cross-fibre strain decreased in magnitude from  $-20.4\%$  to  $-11.8\%$  and from 6.5% to 4.6%, respectively. In the injectate, the maximum and minimum principal strains decreased in magnitude from 5.4% to 0.001% and from  $-5.4\%$  to  $-0.001\%$ , respectively, at end-diastole and from 38.5% to 0.06% and from  $-39.0\%$  to  $-0.06\%$ , respectively, at end-systole. With the microstructural injectate geometry, the developed subject-specific cardiac finite element model offers potential for extension to cellular injectates and in silico studies of mechanotransduction and therapeutic signalling in the infarcted heart with an infarct animal model extensively used in preclinical research.

Email: [dodzi.motchon@uct.ac.za](mailto:dodzi.motchon@uct.ac.za) and  
[thomas.franz@uct.ac.za](mailto:thomas.franz@uct.ac.za)

### Funding information

National Research Foundation of South Africa, Grant/Award Number: IFR14011761118; South African Medical Research Council, Grant/Award Number: SIR328148; CSIR Centre for High Performance Computing, Grant/Award Number: IRMA9543; Dr. Leopold und Carmen Ellinger Stiftung, Grant/Award Number: DAD937134

### KEYWORDS

biomaterial injection therapy, cardiac mechanics, finite element method, myocardial infarction

## 1 | INTRODUCTION

Cardiovascular disease (CVD) is the leading cause of death worldwide. In 2017, CVD was responsible for approximately 17.8 million deaths [1,2]. An increase in CVD-related deaths by 26.9%, from 17.5 million (i.e., 31% of global deaths) in 2012 to 22.2 million by 2030, has been predicted. Alarming, in the working-age population of low- and middle-income countries, including South Africa, the rate of people affected is becoming considerably high [1,3,4]. This situation affects the global economy and therefore influences social cohesion in the communities.

Myocardial infarction (MI) originates from coronary occlusion, causing a lack of oxygenated blood supply to a specific myocardial region. In the long term, cardiomyocyte death is followed by scar formation, causing excessive load to heart dysfunction and heart failure. Current treatments for MI include reperfusion (drug administration or surgery), mechanical device assistance (e.g., left ventricle assist device) and heart transplantation. New therapy approaches based on biomaterial injections have emerged. Clinical studies involving such therapeutic biomaterials showed promising results addressing adverse ventricular remodelling following post-MI inflammatory response [5–8].

Limitations of experimental studies are the cost of resources and the invasiveness of in vivo protocols. Computational modelling appeared as an alternative to investigate the mechanical mechanisms and parameters involved in therapeutic biomaterial injections in infarcted hearts, such as biomaterial stiffness, delivery location, injection volume, and injection pattern [9–16].

Wall et al. [12] reported a reduction in the wall stress, affecting the ventricular function, using an ovine heart finite element (FE) model with a non-contractile biomaterial injectate in the left ventricular (LV) wall implemented by modification of the FE mesh. The results depended on the volume, the location, and the material stiffness of the injected biomaterial.

The morphology and dispersion of the intramyocardial injectates are challenging to control. Wang et al. [13] studied the impact of injectate volume and stiffness on LV myofiber stress and wall thickness. They showed that a larger volume and stiffer material contributes to myofibre stress reduction and wall thickness increase in the LV, which is essential to alter ventricular remodelling. Computational models have been used to optimise the pattern [15,17] and the volume of biomaterial injectates [16].

The current study aimed to develop a biventricular finite element model of a rat heart with an antero-apical infarct and an intramyocardial biomaterial injectate delivered in the infarct region 1 week after infarct induction. A parametric study was undertaken to investigate the effect of injectate stiffness on cardiac mechanics. Emphasis was placed on the realistic microstructural geometrical representation of the in situ intramyocardial dispersion of the biomaterial injectate. The intramyocardial injectate constitutes an important configuration to investigate the mechanical and mechanotransductory responses of therapeutic cells transplanted with the biomaterial for the treatment of myocardial infarction.

## 2 | MATERIALS AND METHODS

### 2.1 | Volumetric image data of infarcted rat heart with intramyocardial injectate

Ex vivo microcomputed tomography ( $\mu$ CT) image data of an infarcted rat heart with polymeric intramyocardial injectate from an unrelated study (unpublished data) were used for geometric reconstruction. In brief, male Wistar rats

(body mass: 180–220 g) were anaesthetized, and the heart was exposed via left thoracotomy along the 4th intercostal space. Myocardial infarction was induced by permanent ligation of the left anterior descending coronary artery 3 mm distal to the auricular appendix. The discolouration of the anterior ventricular wall and reduced contractility were hallmarks of a successful occlusion of the artery. The chest was stepwise closed, and buprenorphine was administered for pain management. Seven days later, the heart was accessed via the 4th intercostal space and 100  $\mu$ L of radiopaque silicone rubber containing lead chromate (Microfil<sup>®</sup> MV-120 Flow-Tech, Carver, MA, USA) diluted 1.5:1 with MV-diluent was injected into the infarct area. Dispersion and in situ polymerisation of the Microfil<sup>®</sup> material were allowed for 30 min after the injection. The animals were then humanely killed, and the hearts were carefully harvested, thoroughly rinsed with saline, fixed in a 4% paraformaldehyde solution and transferred to saline for  $\mu$ CT scanning. All animal experiments were authorised by the Institutional Review Board of the University of Cape Town and performed according to the National Institutes of Health (NIH, Bethesda, MD, USA) guidelines.

The  $\mu$ CT scans were performed with a custom-made scanner with a Feinfocus X-ray tube and a Varian 2520 V Paxscan a-Si flat panel detector (CsI screen,  $1920 \times 1536$ ,  $127 \mu\text{m}$  pixel size) at the Centre for X-ray Tomography of Ghent University (UGCT) [18]. For each scan, 1801 projections were captured with an exposure time of 0.8 s. The resulting scan images had a voxel pitch of  $10 \mu\text{m}$ . Reconstruction was performed using the UGCT software package Octopus [19].

## 2.2 | Three-dimensional reconstruction and meshing of a biventricular cardiac geometry

Only the two ventricles were considered for the FE model, resulting in a biventricular (BV) geometry truncated at the base. Before segmentation, the orientation of the image stack was aligned with the longitudinal cardiac axis. The image segmentation involved region-growing, level-set thresholding and manual segmentation (Simpleware ScanIP, Synopsys). Two masks were created, distinguishing the cardiac tissue and the injectate.

The resulting geometry captured the essential morphology of the left (LV) and right ventricle (RV) and the dispersed intramyocardial injectate in the LV free wall (Figure 1A and Table 1). The geometry was meshed with 206,142 quadratic tetrahedral elements (injectate: 58,902 elements, myocardium: 147,240 elements). The mesh density varied between  $302.8 \text{ mm}^{-3}$  in the myocardium and  $3852.3 \text{ mm}^{-3}$  in the injectate region (Figure 1C).

The meshed geometry was imported in Abaqus 6.14-3 CAE (Dassault Systèmes, Providence, RI, USA). After that, the infarct was approximated in the antero-apical region of the LV and defined as a node set.

## 2.3 | Finite element model development

The meshed BV geometry was imported in Abaqus CAE (Abaqus 6.14-3, Dassault Systèmes, Providence, RI, USA) to implement the different mechanical properties and investigate cardiac tissue mechanics. A 10-node tetrahedral element type (C3D10M) was used to obtain a discretized FE problem.

### 2.3.1 | Myofibre structure

A rule-based approach was used to describe the myofibre angle distribution in the myocardium. A Matlab code developed by Sack et al. [20] was used to generate fibre orientation values through the myocardium. The primary function of the algorithm was to find the different components of the fibre vector within each element in the meshed region of the myocardium. The projected values of the fibre vector were obtained with two principal angles. The helix angle  $\alpha_h$ , is formed by the projection of the fibre on the plane created by the circumferential-longitudinal unit vector ( $u_c$ ,  $u_l$ ) and the circumferential unit vector  $u_c$ . The transverse angle  $\alpha_t$  between the projection of the fibre on the plane is formed by the radial-circumferential unit vector ( $f_{p1}$ ) and the circumferential unit vector. In the current study, the fibre angle was  $-50^\circ$  to  $80^\circ$  from the epicardial to the endocardial surfaces [21,22]. The obtained fibre orientation data were incorporated in the FE model in Abaqus.

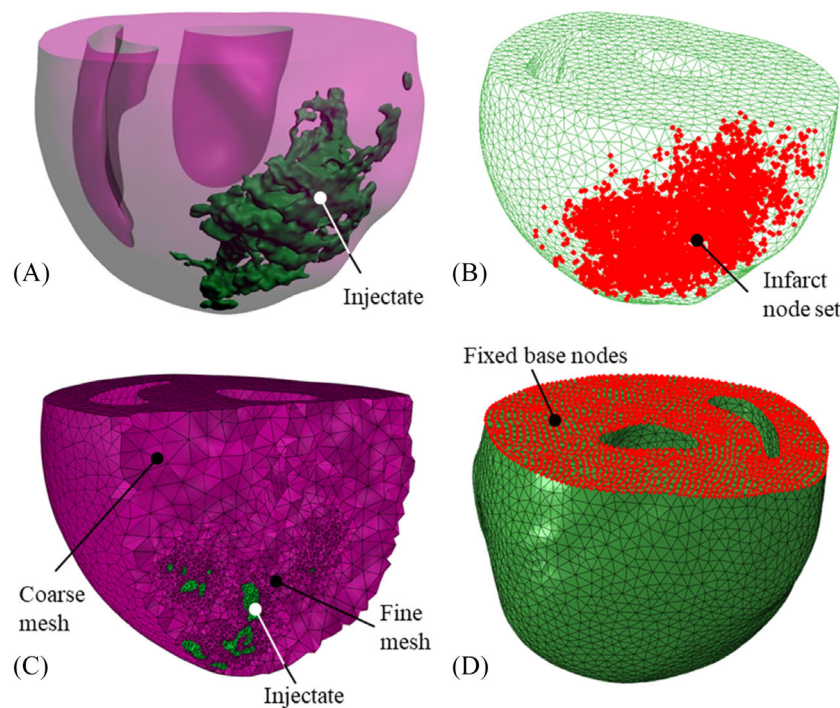


**FIGURE 1** (A) Biventricular cardiac geometry of the rat heart developed from  $\mu$ CT image data with LV, RV, and dispersed intramyocardial injectate in the infarcted region of the LV. (B) Infarct region shown with nodes set, the infarct was defined around the injectate. (C) Increase in mesh density from the myocardium to the injectate to accommodate the microstructural dispersion of the injected material. (D) Nodes on base with boundary condition of zero displacement in the longitudinal direction to prevent rigid body motion (red points).

**TABLE 1** Morphometric data of the biventricular geometry of the rat heart.

Parameter	Value
Myocardial volume ( $\text{mm}^3$ )	1451
LV wall thickness (mm)	4.69–4.93
Septal wall thickness (mm)	2.53–4.54
RV free wall thickness (mm)	1.74–3.24
Apex-base length (mm)	13.94

### 2.3.2 | Constitutive laws

#### *Healthy and infarcted myocardium*

The passive mechanical properties of the myocardium were described with a hyperelastic anisotropic law using a modified strain energy function from Holzapfel and Ogden [23]. The changes were introduced to consider the pathological stage of the heart tissue [20]. The passive mechanical properties of the infarcted myocardium depend on the stage of the infarct [24–27]. A one-week infarct stage was considered in the current study. Hence, an increase in stiffness [28] in the fibre, circumferential and longitudinal direction was implemented with the parameters  $h$  and  $p$  in the Equation (2), with  $h = 1$  and  $0$  representing a healthy and infarcted myocardium, respectively.

$$W = \frac{\bar{a}}{2b} e^{b(I_1-3)} + \sum_{i=f,s} \frac{\bar{a}_i}{2b_i} \left\{ e^{b_i(I_{4i}-1)^2} - 1 \right\} + \frac{\bar{a}_{fs}}{2b_{fs}} \left\{ e^{b_{fs}(I_{8fs})^2} - 1 \right\} + \frac{1}{D} \left( \frac{J^2 - 1}{2} - \ln(J) \right) \quad (1)$$

with

$$\bar{a} = a[h + (1 - h)p],$$

$$\bar{a}_i = a_i[h + (1 - h)p], \text{ and}$$

$$\bar{a}_{fs} = a_{fs}[h + (1 - h)p] \quad (2)$$

The active contraction of the myocardium was implemented with a time-varying elastance approach [29–31], with addition of tissue health parameter  $h$  to represent the pathological stage of the myocardium [20]:

$$T_a(t, E_{ff}) = \frac{T_{\max}}{2} \frac{Ca_0^2}{Ca_0^2 + EC_{a50}^2(E_{ff})} (1 - \cos(\omega(t, E_{ff})))h \quad (3)$$

with

$$EC_{a50}^2(E_{ff}) = \frac{Ca_{0\max}}{\sqrt{e^{B(l(E_{ff}) - l_0)} - 1}}, \quad (4)$$

and

$$\begin{aligned} \omega(t, E_{ff}) &= \pi \frac{t}{t_0}, \text{ for } 0 \leq t \leq t_0 \\ \omega(t, E_{ff}) &= \pi \frac{t - t_0 + t_r(l_r)}{t_r(1)}, \text{ for } t_0 \leq t \leq t_r \\ \omega(t, E_{ff}) &= 0, \text{ for } t \geq t_0 + t_0 \end{aligned} \quad (5)$$

The additive approach was used to determine the total tension in the myocardium where, the time-varying active tension  $T_a$  (Equation (3)) was combined with the tension derived from the passive response,  $T_p$ :

$$T = T_a + T_p \quad (6)$$

The description and values of the passive and active constitutive parameters are provided in Tables S1 and S2.

#### *Injectable biomaterial*

The injectable biomaterial, for example, polyethylene glycol (PEG) hydrogel, was described as hyperelastic isotropic incompressible material with a Neo-Hookean material model:

$$W = C_{10}(I_1 - 3) \quad (7)$$

where  $I_1$  is the first deviatoric strain invariant, and  $C_{10}$  characterises the material stiffness obtained from the elastic modulus  $E_{inj}$  and the Poisson's ratio  $\nu_{inj}$ :

$$C_{10} = \frac{E_{inj}}{4(1 + \nu_{inj})} \quad (8)$$

with  $\nu_{inj} = 0.5$  to represent incompressibility and  $E_{inj}$  between 4.1 and 405,900 kPa (see Section 2.4 Finite element simulations for further details).



### 2.3.3 | Boundary conditions

A zero displacement was applied to the nodes at the base in the longitudinal direction to prevent the rigid body motion of the geometry, see Figure 1D. The passive filling was implemented by a linearly increasing pressure load on both LV and RV cavity surfaces. Several studies reported a higher cavity pressure in the LV than in the RV. In normal human hearts, systolic pressure was 30–40 mmHg in the RV and 100–140 mmHg in the LV [32,33]. Pacher et al. [34] measured left ventricular end-diastolic and end-systolic pressure in rats and found  $3.8 \pm 0.9$  mmHg and  $133.8 \pm 8.1$  mmHg, respectively. In the current study, the cavity pressure was taken from 0 to 3.0 mmHg for the LV and from 0 to 0.75 mmHg for the RV. This choice agrees with the range of the experimental end-diastolic pressure findings.

### 2.3.4 | Determination of computation time for end-systole and end-diastole

The end-diastolic time point was determined by applying a linearly increasing pressure on the LV and RV endocardial surfaces until the LV cavity volume matched a target experimental ED volume by Pacher et al. [34]. This step was performed on the BV model with injectate elastic modulus  $E_{inj} = 73.8$  kPa.

A second simulation was performed to determine the end-systolic time point. The obtained time corresponded to the contraction and was determined from the ED time point defined previously until the active tension declined. The LV volume was calculated at this time point and compared with end-systolic volume values in the literature [34].

## 2.4 | Finite element simulations and data acquisition

A parametric study to determine the impact of the injectate stiffness on the deformation of the myocardium and the biomaterial injectate was conducted with a range of values for the elastic modulus of injectate, that is,  $E_{inj} = 4.1, 7.4, 40.6, 73.8, 405.9, 738, 4059, 7380, 40,590, 73,800$  and  $405,900$  kPa.

The strain in the myocardium and the biomaterial injectate was recorded at the end-diastolic and end-systolic time points of the cardiac cycle for each  $E_{inj}$  value. The myofibre and cross-fibre strains were used for the healthy and infarcted myocardium, whereas the maximum principal and minimum principal strains were used for the injectate. The ex vivo geometry of the heart developed from  $\mu$ CT image data was used as reference configuration for strain calculations. This configuration was assumed unloaded, and pre-stress was not considered.

For each finite element in the mesh, the element strain,  $\epsilon_{EL}$ , was determined as the arithmetic mean of the strain values at the four integration points,  $\epsilon_{IP,i}$ , of the 10-node tetrahedral elements.

## 2.5 | Statistical analysis

Descriptive statistical analysis was performed on the strain data to determine the normality (Shapiro–Wilk normality test) and variability (SciPy, <https://scipy.org/> and NumPy, <https://numpy.org/>). Data were presented using box and whisker plots (Matplotlib, Python, <https://matplotlib.org/>) indicating median and interquartile ranges.

## 3 | RESULTS

Representative end-diastolic and end-systolic strain distributions are shown for the myofibre and cross-fibre strain in the BV wall in Figure 2 and the maximum and minimum principal strain in the injectate in Figure 3, for an elastic modulus of the injectate of  $E_{inj} = 73.8$  kPa.

### 3.1 | Effect of injectate stiffness on myocardial deformation

The median end-diastolic myofibre and cross-fibre strain decreased from 3.5% to 1.0% and  $-5.9\%$  to  $-2.7\%$  (decrease in magnitude) for the increase in the injectate elastic modulus (Figure 4A,B). These changes in strain

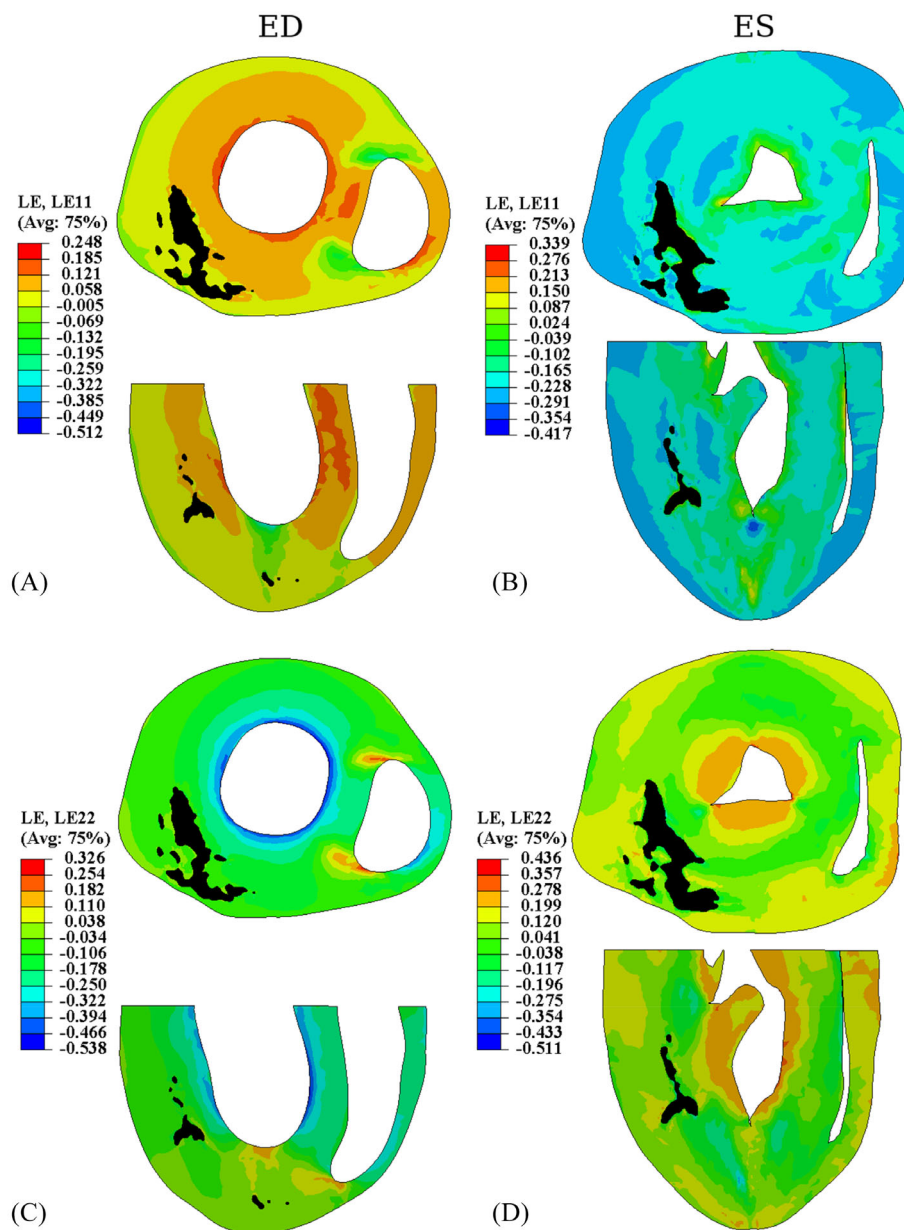


**FIGURE 2** Short-axis and longitudinal contour plots showing myofibre strain (A, B) and cross-fibre strain (C, D) in the BV model at end-diastolic (ED, left column) and end-systolic time point (ES, right column) for an injectate elastic modulus  $E_{inj} = 73.8$  kPa. The strain distribution in the injectate (black areas) is shown in Figure 3.

appear to be more pronounced in the low modulus region  $E_{inj} = 4.1$  to 738 kPa and only marginal for  $E_{inj} > 738$  kPa.

At end-systole, the median myofibre strain decreased in magnitude from  $-20.4\%$  to  $-11.8\%$ , with increasing elastic modulus. The median cross-fibre strain decreased from  $6.5\%$  to  $4.6\%$  with an increasing elastic modulus with an intermittent marginal increase for  $E_{inj} = 405.9$  kPa and 738.0 kPa (Figure 4C,D).

### 3.2 | Effect of injectate stiffness on injectate deformation

As a general observation, the magnitude (i.e., median), range (difference between the highest and lowest element strain) and interquartile range of maximum and minimum principal strain decreased considerably with increasing

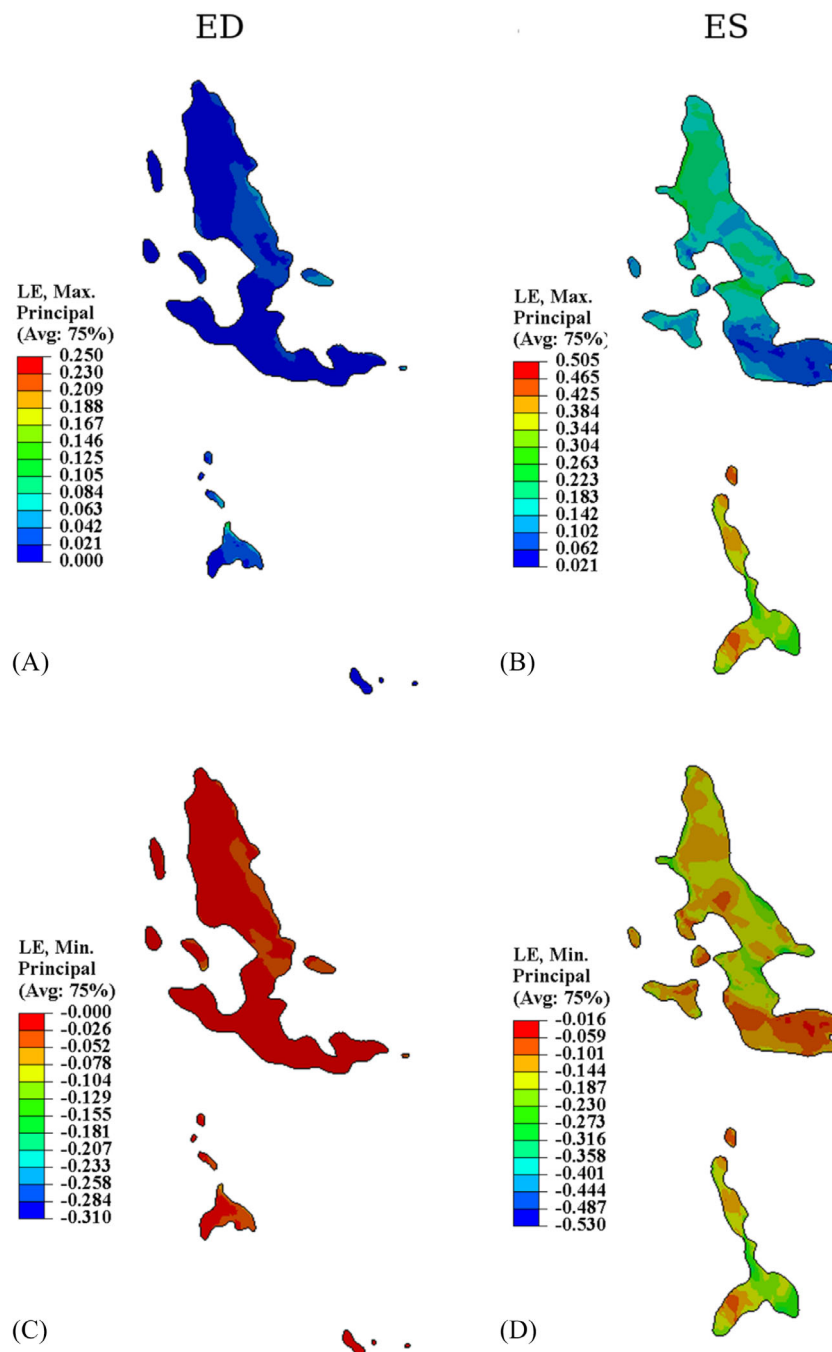


**FIGURE 3** Short-axis and longitudinal contour plots of maximum (A, B) and minimum principal strain (C, D) in the injectate at end-diastolic (ED, left column) and end-systolic time point (ES, right column) for an injectate elastic modulus  $E_{inj} = 73.8$  kPa.

injectate stiffness for lower  $E_{inj} = 4.1$ – $738$  kPa. However, the strain decreased marginally for the higher  $E_{inj} = 4059$  to  $405,900$  kPa, both at end-diastolic and end-systolic time points.

At end-diastole, the median maximum principal strain decreased from  $5.4\%$  to  $0.001\%$ , and the median minimum principal strain decreased in magnitude from  $-5.4\%$  to  $-0.001\%$  for increasing injectate stiffness (Figure 5A,B).

At end-systole, the median maximum principal strain decreased from  $38.5\%$  to  $0.06\%$ , and the median minimum principal strain decreased in magnitude from  $-39.0\%$  to  $-0.06\%$  with increasing injectate stiffness (Figure 5C,D).



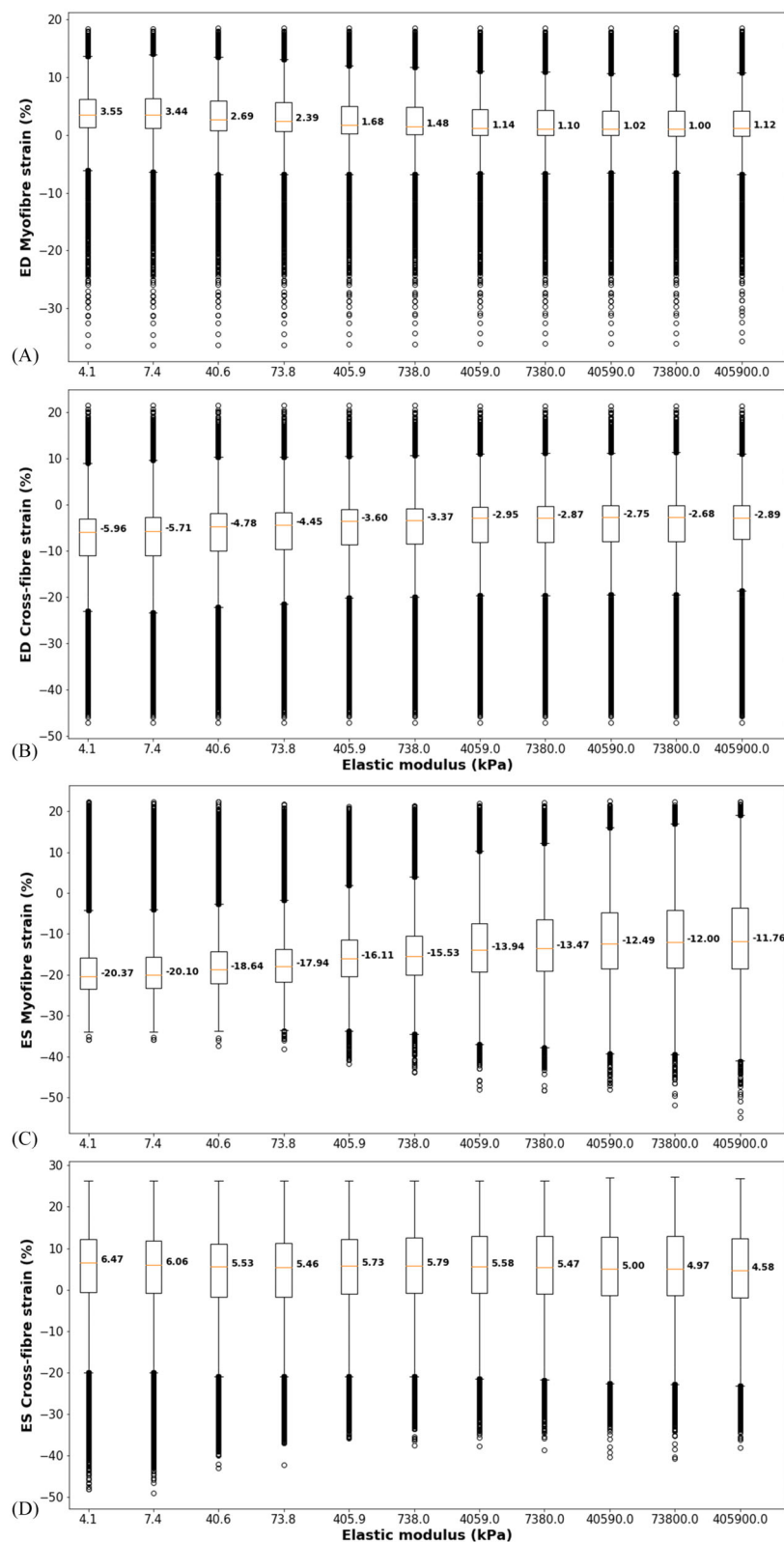


**FIGURE 4** Myocardial deformation. End-diastolic (ED) myofibre (A) and cross-fibre (B) strain and end-systolic (ES) myofibre (C) and cross-fibre (D) strain versus injectate elastic modulus. The box and whiskers indicate the median (red line in box), interquartile range (IQR) from first and third quartile (lower and upper bound of the box),  $1.5 \times$  IQR (lower and upper whisker), and data larger or smaller than  $1.5 \times$  IQR (open circles). Each data point represents the strain value  $\epsilon_{EL}$  in an element of the finite element mesh. Data larger or smaller than  $1.5 \times$  IQR are not considered outliers but true data.

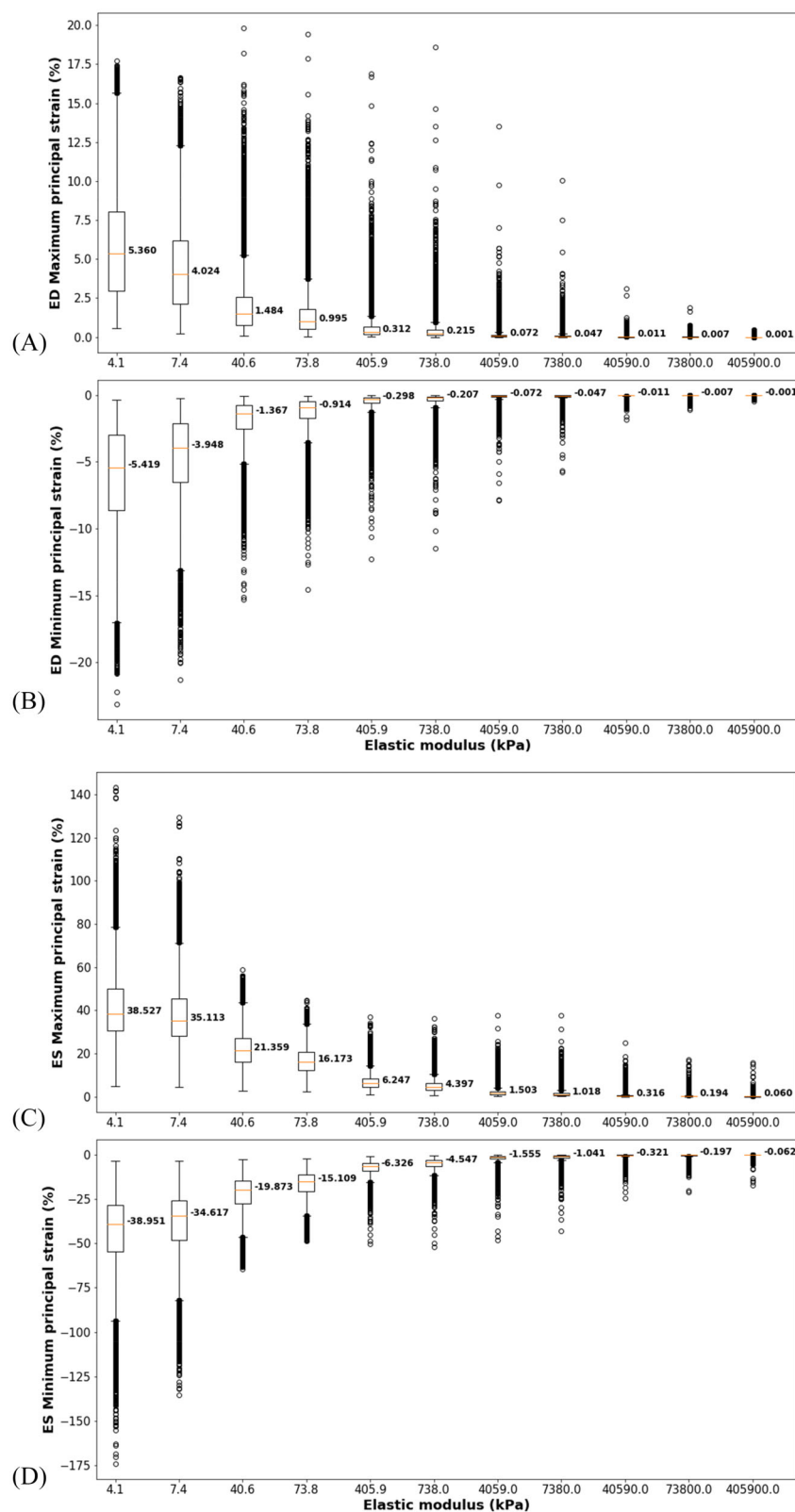


**FIGURE 5** Injectate deformation. End-diastolic (ED) maximum (A) and minimum (B) principal strain and end-systolic (ES) maximum (C) and minimum (D) principal strain. The box and whiskers indicate the median (red line in box), interquartile range (IQR) from the first and third quartile (lower and upper bound of the box),  $1.5 \times$  IQR (lower and upper whisker), and data larger or smaller than  $1.5 \times$  IQR (open circles). Each data point represents the strain value  $\varepsilon_{EL}$  in an element of the finite element mesh. Data larger or smaller than  $1.5 \times$  IQR are not considered outliers but true data.

## 4 | DISCUSSION

The present computational study involved the development of computational models for cardiac mechanics. The effect of the therapeutic biomaterial injectate stiffness on the cardiac mechanics during a cardiac cycle was shown using the developed models. At a given injectate elastic modulus, the end-diastolic myofibre strain decreased from the endocardial to the epicardial surface, which has also been reported in other studies [35–37]. The biomaterial delivery 7 days after infarct induction was chosen since significant improvements in cardiac function and scar tissue mechanics were reported in vivo for the injection of PEG hydrogel 1 week following the infarction compared to biomaterial delivery immediately after the infarction [38].

Many computational studies involving animal species used simplified cardiac geometries [12,15,39]. The current study was the first to develop a subject-specific biventricular geometry of a rat heart with in situ microstructural details of an intramyocardial injectate in the LV free wall. This detailed representation of the injectate is important for investigating the mechanics and mechanotransduction of cells delivered with and embedded in the biomaterial to advance cell therapies for myocardial infarction. The morphological details at the micrometre length scale resulted in a considerably higher and more heterogeneous mesh density.

The reconstruction of the biventricular FE model used a validated method developed in one of our previous studies [20]. That study included an assessment of the mesh sensitivity, and although the mesh convergence analysis was not reported, mesh sensitivity guidelines for biventricular models were established. For quadratic tetrahedral elements, a mesh density of approximately 40,000 elements was sufficient to reach convergence of stress, strain and hemodynamic performance. The model used in the current study exceeds 200,000 elements, a deliberately fine resolution mesh, and a mesh sensitivity assessment was not deemed necessary.

Different strain energy density functions were used for the discrete representation of myocardial and injectate regions, contrary to studies that used the homogenisation approach that combines the myocardium and biomaterial injectate [12,14]. This approach allowed capturing the distinctly different mechanical properties of the myocardium and injected biomaterial.

The current study adopted passive myocardial material parameters from Dương et al. [40], who developed and validated the constitutive model for infarcted rat myocardium with experimental data from biaxial tension and uniaxial compression [41]. The active contraction in the healthy myocardial regions was modelled with a validated time-varying elastance model [30]. The parameters estimated by Guccione et al. [30] have been used in several computational studies involving rat [16] and porcine models [20].

Therapeutic intramyocardial biomaterial injectates with different mechanical properties have been reported to induce different mechanical and functional responses in the infarcted heart [12].

The current study showed that an increasing elastic modulus (i.e., stiffness) of the biomaterial injectate reduces the ES and ED myocardial strains in the myofibre and cross-fibre directions in the healthy and infarcted regions of the BV geometry. This finding suggests that an increasing elastic modulus of the injectate for MI treatment may result in a beneficial effect of reducing the myocardial strains in the remote healthy regions of the BV geometry.

The biomaterial injectate is often used as a scaffold for therapeutically delivered cells for MI treatment. Thus, investigating the mechanical response of the biomaterial injectate delivered to the infarct is crucial for embedded cells' mechanics and associated signalling. The current study showed that the mechanical response of the injectate depends on its stiffness. The maximum and minimum principal strains decreased for an increasing injectate elastic modulus. The upper range of the injectate's elastic modulus (i.e.,  $E_{inj} > 738$  kPa) used in the study is unrealistic for PEG hydrogels and other injectable biomaterials [42,43]. However, the current investigations aimed to explore the injectate response for an extensive range of injectate stiffness, and it was shown that the injectate deformations were negligible for these unrealistically high values of the injectate elastic modulus.

Limitations of the current study include the simplifying assumption of the ex vivo cardiac geometry reconstructed from  $\mu$ CT data as unloaded reference configuration for strain quantification.

The continuous mesh used for the myocardium and biomaterial injectate resulted in tied contact properties at the domain interfaces. More realistic contact interactions between myocardium and biomaterial will improve the simulation of the mechanics of the interface and the injectate but require experimental data that currently do not exist.

Considering the impact of the injectate stiffness on the ED and ES time point may improve the model's accuracy. Furthermore, additional parameters such as injectate location and different injectate patterns may be considered to investigate their effect on the infarcted heart.

A linearly increasing pressure load on the cavity surfaces was used to implement the passive filling. This simple approach can be improved by using a more comprehensive representation of the circulatory system, including systemic arteries and veins, a pulmonary circuit, and the heart's upper chambers and valves, as described by Sack et al. [20].

The model's anatomical details can be enhanced by implementing fibre orientation in the subject-specific biventricular geometry based on diffusion tensor magnetic resonance imaging.

## 5 | CONCLUSIONS

This is the first computational study that generated and used a high-resolution microstructurally geometry of an in situ biomaterial injectate delivered 1 week after infarct induction in a biventricular cardiac finite element model of a rat heart with antero-apical infarct in the left ventricular free wall. With the microstructurally detailed in situ injectate geometry, the computational model of an infarcted rat heart offers vast potential for in silico studies of mechanotransduction and therapeutic signalling of cells transplanted with deliverable biomaterials in the infarcted heart, an animal model that has been extensively used in preclinical research of myocardial infarction.

### NOMENCLATURE

$a$	material parameter, dimension of stress
$a_{fs}$	material parameter defining coupling from in the fibre and sheet directions, with a dimension of stress
$a_i$	material parameter, defined for $i = f$ and $s$ in the fibre and sheet directions, respectively, with stress dimension
$\bar{a}, \bar{a}_i, \bar{a}_{fs}$	govern the isotropic response of the infarcted myocardium
$B$	governs the shape of peak isometric tension-sarcomere length relation
$b$	dimensionless material parameter in Holzapfel model
$b_{fs}$	material parameter defining coupling from in the fibre and sheet directions, dimensionless
$b_i$	material parameter, defined for $i = f$ and $s$ in the fibre and sheet directions, respectively, dimensionless
$C_{10}$	coefficient used in Abaqus to describe the material stiffness in a Neo-Hookean strain energy density function
$Ca_0$	peak intracellular calcium concentration
$D$	parameter for elastic materials defining the compressibility of the material
$E$	elastic modulus
$E Ca_{50}$	length-dependent calcium sensitivity
$h$	parameter to define the pathological degree of the tissue
$I_{4f}$	transversely isotropic invariant in the fibre direction
$I_{4s}$	transversely isotropic invariant in the sheet direction
$I_{8fs}$	orthotropic invariant from coupling in fibre and sheet direction
$I_i$	isotropic invariants in principal directions
$J$	third deformation gradient invariant as measures of the volume change of compressible materials
$p$	parameter scaling the isotropic response of the diseased tissue
$T$	stress tensor
$T^{(a)}$	active stress tensor
$T^{(p)}$	passive stress tensor
$u_c$	unit vector in the circumferential direction
$u_l$	unit vector in the longitudinal direction
$W$	strain energy density function
$\alpha_h$	helix angle
$\alpha_t$	transverse angle
$\varepsilon_{EL}$	element strain; mean value of strains at integration points in an element
$\varepsilon_{IP,i}$	strain at integration point $i$ in an element with $i = 1$ to $4$
$\nu$	Poisson's ratio
$\sigma$	stress

## FUNDING INFORMATION

This work was supported by financially supported by the National Research Foundation of South Africa (IFR14011761118 to TF), the South African Medical Research Council (SIR328148 to TF), and the CSIR Centre for High Performance Computing (CHPC Flagship Project Grant IRMA9543 to TF), and the Dr. Leopold und Carmen Ellinger Stiftung (UCT Three-Way PhD Global Partnership Programme Grant DAD937134 to TF). The funders had no role in study design, data collection and analysis, decision to publish, or preparation of the manuscript. Any opinion, findings, conclusions, and recommendations expressed in this publication are those of the authors, and therefore, the funders do not accept any liability.

## CONFLICT OF INTEREST

The authors declare no conflict of interest.

## DATA AVAILABILITY STATEMENT

Data supporting the results presented in this article are available on the University of Cape Town's institutional data repository (ZivaHub) under <http://doi.org/10.25375/uct.19630203> as Y. D. Motchon, Kevin L. Sack, M. S. Sirry, E. Pauwels, D. Van Loo, A. De Muynck, L. Van Hoorebeke, Neil H. Davies, Thomas Franz. Effect of biomaterial stiffness on cardiac mechanics in a biventricular infarcted rat heart model with microstructural representation of in situ intramyocardial injectate. Cape Town, ZivaHub, 2022, DOI: <http://doi.org/10.25375/uct.19630203>.

## ORCID

Thomas Franz  <https://orcid.org/0000-0002-1504-3842>

## REFERENCES

- Kaptoge S, Pennells L, De Bacquer D, et al. World health organization cardiovascular disease risk charts: revised models to estimate risk in 21 global regions. *Lancet: Glob Health*. 2019;7(10):e1332-e1345.
- Mendis S, Puska P, Norrving B. *Global Atlas on Cardiovascular Disease Prevention and Control*. World Health Organization; 2011.
- Finegold JA, Asaria P, Francis DP. Mortality from ischaemic heart disease by country, region, and age: Statistics from World Health Organisation and United Nations. *Int J Cardiol*. 2013;168(2):934-945.
- Opie LH, Mayosi BM. Cardiovascular disease in sub-saharan africa. *Circulation*. 2005;112(23):3536-3540.
- Christman KL, Fok HH, Sievers RE, Fang Q, Lee RJ. Fibrin glue alone and skeletal myoblasts in a fibrin scaffold preserve cardiac function after myocardial infarction. *Tissue Eng*. 2004;10(3-4):403-409.
- Fan C, Shi J, Zhuang Y, et al. Myocardial-infarction-responsive smart hydrogels targeting matrix metalloproteinase for on-demand growth factor delivery. *Adv Mater*. 2019;31(40):e1902900.
- Johnson TD, Christman KL. Injectable hydrogel therapies and their delivery strategies for treating myocardial infarction. *Expert Opin Drug Deliv*. 2013;10(1):59-72.
- Silveira-Filho LM, Cayan GN, Adamo A, et al. Can a biohybrid patch salvage ventricular function at a late time point in the post-infarction remodeling process? *Basic Transl Sci*. 2021;6(5):447-463.
- Cai L, Wang Y, Gao H, Li Y, Luo X. A mathematical model for active contraction in healthy and failing myocytes and left ventricles. *PLoS One*. 2017;12(4):e0174834.
- Kortsmit J, Davies NH, Miller R, Macadangdang JR, Zilla P, Franz T. The effect of hydrogel injection on cardiac function and myocardial mechanics in a computational post-infarction model. *Comput Methods Biomech Biomed Eng*. 2013;16(11):1185-1195.
- Kortsmit J, Davies NH, Miller R, Zilla P, Franz T. Computational predictions of improved of wall mechanics and function of the infarcted left ventricle at early and late remodelling stages: comparison of layered and bulk hydrogel injectates. *Advances in Biomechanics and Applications*. 2013;1(1):41-55.
- Wall ST, Walker JC, Healy KE, Ratcliffe MB, Guccione JM. Theoretical impact of the injection of material into the myocardium: a finite element model simulation. *Circulation*. 2006;114(24):2627-2635.
- Wang H, Rodell CB, Lee ME, et al. Computational sensitivity investigation of hydrogel injection characteristics for myocardial support. *J Biomech*. 2017;64:231-235.
- Wenk JF, Eslami P, Zhang Z, et al. A novel method for quantifying the in-vivo mechanical effect of material injected into a myocardial infarction. *Ann Thorac Surg*. 2011;92(3):935-941.
- Wenk JF, Wall ST, Peterson RC, et al. A method for automatically optimizing medical devices for treating heart failure: designing polymeric injection patterns. *J Biomech Eng*. 2009;131(12):121011.
- Wise P, Davies NH, Sirry MS, et al. Excessive volume of hydrogel injectates may compromise the efficacy for the treatment of acute myocardial infarction. *Int J Numer Methods Biomed Eng*. 2016;32(12):e02772.
- Sepantafar M, Maheronnaghsh R, Mohammadi H, et al. Stem cells and injectable hydrogels: synergistic therapeutics in myocardial repair. *Biotechnol Adv*. 2016;34(4):362-379.



18. Masschaele BC, Cnudde V, Dierick M, Jacobs P, Van Hoorebeke L, Vlassenbroeck J. Ugct: new x-ray radiography and tomography facility. *Nucl Instrum Methods Phys Res, Sect A*. 2007;580(1):266-269.
19. Vlassenbroeck J, Dierick M, Masschaele B, Cnudde V, Van Hoorebeke L, Jacobs P. Software tools for quantification of x-ray microtomography at the ugct. *Nucl Instrum Methods Phys Res, Sect A*. 2007;580(1):442-445.
20. Sack KL, Aliotta E, Ennis DB, et al. Construction and validation of subject-specific biventricular finite-element models of healthy and failing swine hearts from high-resolution DT-MRI. *Front Physiol*. 2018;9(539):539.
21. Chen J, Song S-K, Liu W, et al. Remodeling of cardiac fiber structure after infarction in rats quantified with diffusion tensor mri. *Am J Physiol-Heart Circ Physiol*. 2003;285(3):H946-H954.
22. Sirry MS. *Computational Biomechanics of Acute Myocardial Infarction and its Treatments*. Human Biology, Univerity of Cape Town; 2015:145.
23. Holzapfel GA, Ogden RW. Constitutive modelling of passive myocardium: a structurally based framework for material characterization. *Philos Trans A Math Phys Eng Sci*. 2009;367(1902):3445-3475.
24. Holmes JW, Borg TK, Covell JW. Structure and mechanics of healing myocardial infarcts. *Annu Rev Biomed Eng*. 2005;7:223-253.
25. Holmes JW, Nunez JA, Covell JW. Functional implications of myocardial scar structure. *Am J Physiol*. 1997;272(5 Pt 2):H2123-H2130.
26. Tyberg JV, Forrester JS, Wyatt HL, Goldner SJ, Parmley WW, Swan HJ. An analysis of segmental ischemic dysfunction utilizing the pressure-length loop. *Circulation*. 1974;49(4):748-754.
27. Villarreal FJ, Lew WY, Waldman LK, Covell JW. Transmural myocardial deformation in the ischemic canine left ventricle. *Circ Res*. 1991;68(2):368-381.
28. Hood WB, Bianco JA, Kumar R, Whiting RB. Experimental myocardial infarction: iv. Reduction of left ventricular compliance in the healing phase. *J Clin Invest*. 1970;49(7):1316-1323.
29. Guccione J, McCulloch A. Mechanics of active contraction in cardiac muscle: part i—constitutive relations for fiber stress that describe deactivation. *J Biomech Eng*. 1993;115(1):72-81.
30. Guccione J, Waldman L, McCulloch A. Mechanics of active contraction in cardiac muscle: part ii—cylindrical models of the systolic left ventricle. *J Biomech Eng*. 1993;115(1):82-90.
31. Walker JC, Ratcliffe MB, Zhang P, et al. Mri-based finite-element analysis of left ventricular aneurysm. *Am J Physiol Heart Circ Physiol*. 2005;289(2):H692-H700.
32. Mininni S, Diricatti G, Vono MC, et al. Noninvasive evaluation of right ventricle systolic pressure during dynamic exercise by saline-enhanced doppler echocardiography in progressive systemic sclerosis. *Angiology*. 1996;47(5):467-474.
33. Reichek N, Devereux RB. Reliable estimation of peak left ventricular systolic pressure by m-mode echographic-determined end-diastolic relative wall thickness: identification of severe valvular aortic stenosis in adult patients. *Am Heart J*. 1982;103(2):202-203.
34. Pacher P, Mabley JG, Liaudet L, et al. Left ventricular pressure-volume relationship in a rat model of advanced aging-associated heart failure. *Am J Physiol Heart Circ Physiol*. 2004;287(5):H2132-H2137.
35. Costa KD, Takayama Y, McCulloch AD, Covell JW. Laminar fiber architecture and three-dimensional systolic mechanics in canine ventricular myocardium. *Am J Physiol*. 1999;276(2):H595-H607.
36. Takayama Y, Costa KD, Covell JW. Contribution of laminar myofiber architecture to load-dependent changes in mechanics of lv myocardium. *Am J Physiol Heart Circ Physiol*. 2002;282(4):H1510-H1520.
37. Waldman LK, Nosan D, Villarreal F, Covell JW. Relation between transmural deformation and local myofiber direction in canine left ventricle. *Circ Res*. 1988;63(3):550-562.
38. Kadner K, Dobner S, Franz T, et al. The beneficial effects of deferred delivery on the efficiency of hydrogel therapy post myocardial infarction. *Biomaterials*. 2012;33(7):2060-2066.
39. Dieudonné J-M. The left ventricle as confocal prolate spheroids. *Bull Math Biophys*. 1969;31(3):433-439.
40. Duong MTN, Ach T, Alkassar M, Dittrich S, Leyendecker S. Numerical simulation of cardiac muscles in a rat biventricular model. In: Paper presented at: 6th European Conference on Computational Mechanics (ECCM 6), 7th European Conference on Computational Fluid Dynamics (ECFD 7), UK; 2018.
41. Sirry MS, Butler JR, Patnaik SS, et al. Characterisation of the mechanical properties of infarcted myocardium in the rat under biaxial tension and uniaxial compression. *J Mech Behav Biomed Mater*. 2016;63:252-264.
42. Rizzi SC, Ehrbar M, Halstenberg S, et al. Recombinant protein-co-peg networks as cell-adhesive and proteolytically degradable hydrogel matrixes. *Part II: Biofunct Charact Biomacromol*. 2006;7(11):3019-3029.
43. Singelyn JM, Sundaramurthy P, Johnson TD, et al. Catheter-deliverable hydrogel derived from decellularized ventricular extracellular matrix increases endogenous cardiomyocytes and preserves cardiac function post-myocardial infarction. *J Am Coll Cardiol*. 2012;59(8):751-763.

## SUPPORTING INFORMATION

Additional supporting information can be found online in the Supporting Information section at the end of this article.

**How to cite this article:** Motchon YD, Sack KL, Sirry MS, et al. Effect of biomaterial stiffness on cardiac mechanics in a biventricular infarcted rat heart model with microstructural representation of in situ intramyocardial injectate. *Int J Numer Meth Biomed Engng*. 2023;39(5):e3693. doi:[10.1002/cnm.3693](https://doi.org/10.1002/cnm.3693)